ELSEVIER

Contents lists available at ScienceDirect

International Journal of Heat and Fluid Flow

journal homepage: www.elsevier.com/locate/ijhff





Characterization of compressible flow through microscale orifice arrays

Nathan P. Hagstrom *, Matthew L. Gallagher, Thomas R. Chase

University of Minnesota - Twin Cities, Department of Mechanical Engineering, 111 Church Street SE, Minneapolis, 55455, MN, United States

ARTICLE INFO

Keywords:
Orifice
Discharge coefficient
Compressible flow

ABSTRACT

Compressible flow through arrays of circular micro-orifices was experimentally and numerically studied to better understand how the characteristic dimensions of micro-orifices used in macroscale fluidic systems using a plurality of micro-orifices impacts discharge coefficient. The studies were carried out with micro-orifice diameters ranging from 125 μ m to 1000 μ m, with the number of micro-orifices in an array ranging from 2 to 64, and at gauge inlet pressures ranging from 25 to 600 kPa venting to atmospheric pressure. Results showed that micro-orifice diameter to thickness aspect ratio and wall profile were significant factors in determining discharge coefficient. The number of micro-orifices in a system was found to have negligible impact on discharge coefficient so long as the micro-orifices were separated by two diameters or more. When this spacing was maintained, two dimensional axisymmetric micro-orifice numerical studies produced discharge coefficients that agreed well with experimental data gathered on three dimensional micro-orifice arrays. The micro-orifice arrays produced discharge coefficients as high as 0.997 using photochemically etched micro-orifices, 0.981 using silicon etched micro-orifices, and 0.831 with drilled micro-orifices.

1. Introduction

Integration of microtechnology into flow control systems demands an intimate working knowledge of the relationship between shrinking characteristic length scales and system performance. As such, significant research efforts have focused on the performance of microscale flow elements in microfluidic systems. Previously noted applications for microscale flow elements include: micropropulsion (Mueller et al., 2000; Yang et al., 2004), bioMEMS (Au et al., 2011; Galambos et al., 2011), refrigeration (Park et al., 2009, 2008), and numerous microvalves (Shoji and Esashi, 1994; Zhang et al., 2007; Oh and Ahn, 2006; Vandelli et al., 1998; Saha et al., 2007; Su et al., 2015). Success of and ability to fabricate devices working on this length scale have been driven by continual advances in microfabrication techniques.

The improvements in manufacturing techniques have made it practical to scale technology such as micro-orifices for use in larger fluidic systems operating at the millimeter scale or greater. Potential benefits of using micro-orifices in larger scale liquid and gaseous based systems include: turbulence rejection (Huang et al., 2013), reduced rates of cavitation (Jin et al., 2019; Cioncolini et al., 2016), reduced viscous energy losses (Aly et al., 2010), and increased flow capacity in miniature valves (Hagstrom et al., 2019). The relevant literature on study of orifice flow, micro-orifice flow, and optical flow analysis is reviewed in the following subsections.

1.1. Background: Orifice flow characterization

Microscale orifices or micro-orifices have been widely studied in the literature with a focus on liquid based systems. Recent research on micro-orifices have studied their potential to act as efficient structures for inducing or reducing hydrodynamic cavitation (Jin et al., 2019; Cioncolini et al., 2016). Other research studied the impact of straight drilled micro-orifice diameter and aspect ratio on resultant discharge coefficient (Cioncolini et al., 2018, 2015). In liquid based systems, Cioncolini et al. found the aspect ratio of a micro-orifice to have little impact on discharge coefficient (Cioncolini et al., 2018). It was instead determined that discharge coefficient was primarily a function of Reynolds number. Further study is warranted to determine the degree that this behavior extends to compressible flow.

Huang et al. studied the impact of using an array of orifices as a liquid flow meter in comparison to a single orifice (Huang et al., 2013). Their work found that an array of orifices with summative equivalent area to a single orifice was able to increase system discharge coefficient, but without an identifiable empirical relationship. The identified increase in discharge coefficient related to orifice array use was specific to use of a liquid medium. Use of a gaseous medium as opposed to a

E-mail address: hagst082@umn.edu (N.P. Hagstrom).

Corresponding author.

liquid is likely to impact this finding given the change in relationship between inertial forces and viscous forces in addition to compressibility effects.

Work focused on study of orifice flow at the millimeter scale using a gaseous medium centered on quantifying flow rate as a function of orifice aspect ratio and edge geometry. Alam et al. experimentally and numerically studied the effect of inlet and exit edge geometry on orifice flow with a nominal diameter of 12.7 mm. Shadowgraphy was used to validate the numerical models and also to analyze shock formation. Results showed that inlet edge geometry was a significant factor in determining discharge coefficients (Alam et al., 2016). Aly et al. experimentally studied the impact of using fractal shaped orifices in opposition to circular orifices (Aly et al., 2010). Their study found that fractal patterns with equal flow area to circular orifices were able to reduce the pressure drop across the orifice. These results are expected to translate from millimeter scale orifices to microscale orifices.

While a majority of work studying orifice flow to date has been performed on millimeter scale or larger orifices, some work has been conducted in the microscale realm. One such work by Mishra et al. investigated flow through rectangular silicon etched micro-orifices with both compressible and incompressible fluids (Mishra and Peles, 2005b). The primary aim of this work was to expand study of micro-orifice discharge coefficients further into the microscale using rectangular micro-orifices with throat widths ranging from 11.5 μm to 40 μm and a throat height of 101.3 µm. Their research identified that when using compressible fluids, micro-orifices behave like micronozzles with discharge coefficients trending towards unity past the critical pressure ratio. Using the same micro-orifice geometry as in Mishra and Peles (2005b), Mishra et al. studied the cavitation behaviors of liquids flowing at large Reynolds numbers (Mishra and Peles, 2005a). In other similar work, Asako et al. (2003) studied the impact of fluid compressibility on flow through microchannels. The result was an empirical relationship between friction factor and Mach number for compressible flow through microchannels.

Kayser et al. researched the orifice discharge coefficient as a function of edge geometry with diameters ranging from 0.893 mm to 1.890 mm (Kayser and Shambaugh, 1991). Results showed that edge geometry modification at this length scale was a large factor in modeling the discharge coefficient whereas the orifice diameter played a much lesser role. Previous work by Hagstrom et al. found compressible flow through an array of etched silicon circular micro-orifices, 64×160 μ m, achieved an average discharge coefficient of 0.89 at choked conditions with pressure differences up to 600 kPa (Hagstrom et al., 2019). The results from Hagstrom et al. (2019) warranted further study to better understand the impact of orifice array design on discharge coefficient and are further studied within this work.

1.2. Background: Microscale flow visualization

Optical study of inhomogeneities present in transparent fluid media is known as schlieren imaging. It is believed that the first documented use of an optical system to visualize transparent flow dates back to the late 1660's (Rienitz, 1975). Three centuries later, more in depth documentation appeared where Vogt published his design of a simple two lens schlieren system (Vogt, 1957). Most recent popularization of schlieren imaging and other derivative methods was galvanized by Settles and Klein in the early 2000's (Settles, 2001; Kleine, 2001). Since, there have been advances in imaging and optical technology that allowed for development of increasingly complex methods for flow visualization (Settles and Hargather, 2017). Advances have focused on a few main areas including: image processing, complex three dimensional analysis methods, and imaging at the microscale. Use of schlieren imaging as it pertains to this work focused largely on study of micronozzles and microthrusters.

One of the earliest examples of microjet imaging was presented by Scroggs and Settles (1996). Their work studied the shock cell structure and pressure distribution of microjets created by micronozzles with exit diameters from 600 μm to 1200 μm . Since, many others have studied microjet shock structure and periodicity with micronozzle diameters from 10.4 μm to 1000 μm (Nazari et al., 2020; Bharadwaja et al., 2019; Wright and Syms, 2018; Aniskin et al., 2013; Lekholm et al., 2012, 2011; Phalnikar et al., 2008). Central conclusions drawn from these works were that shock cell period is a function of throat diameter, source temperature, and pressure difference.

Previous work has shown that relatively simple two lens schlieren systems provide sufficient magnification and resolution to properly image microjets (Lekholm et al., 2012, 2011; Huang et al., 2007a,b). Cold gas microthrusters were studied by Lekholm et al. (2012, 2011). In this work, silicon microthrusters with a rectangular cross-section were etched using DRIE. They were able to image the outlet of a micronozzle measuring 20 μm at the throat and 350 μm at the outlet. Huang et al. studied a CNC machined micronozzle with a rectangular throat width of 254 μm and an outlet width of 1046 μm (Huang et al., 2007a,b). They were able to visualize the shock cell structure at the micronozzle exit. They used a background image subtraction method to improve analysis sensitivity, which is also utilized in Section 4.2.

1.3. Motivation

Use of micro-orifices can benefit larger scale fluidic systems. However, in larger systems, a plurality of micro-orifices are required to maintain system output due to the small flow capacity afforded by a single micro-orifice. These larger systems would require use of a micro-orifice array. A gap in the literature exists for study of such systems that utilize a gaseous fluid, making informed design difficult. Deeper understanding of flow through micro-orifice arrays is needed to define the relationship between flow capacity and micro-orifice array design parameters. Relevant micro-orifice design parameters include: number, diameter to thickness aspect ratio, and wall profile.

The objectives of this work are threefold. The primary objective is to provide a body of experimental flow characterization data to improve understanding of micro-orifice array flow capacity when using a gaseous working fluid. The second objective is to present a simple method for numerically modeling a three dimensional array of microorifices to corroborate the aforementioned experimental data and provide deeper insights into the physics of flow through a micro-orifice. The last objective is to provide schlieren imaging based data on microorifice jetting profiles and shock formation for use in validating the created numerical models. Comparison between the numerical modeling, schlieren images, and experimental data will provide rationale for numerically modeling just one of an array of N micro-orifices using axisymmetric elements; e.g., interaction between orifices is insignificant for realistic orifice spacing. This rationale in combination with the empirical relationships developed for the studied micro-orifices will enable informed design of systems using micro-orifice arrays.

In the following section, the theoretical background for microorifice flow and schlieren imaging are first introduced. Second, the experimental flow characterization system and numerical domains are described. After, the results from the experimental and numerical studies are reviewed. Then, the results are discussed. In the last section the conclusions are presented.

2. Theoretical background

This section provides theoretical context for work completed in subsequent sections. The theoretical background for experimental compressible micro-orifice flow rate characterization is first described. After which, the underpinnings of schlieren optical flow analysis and system design are detailed to inform straightforward implementation of two lens based schlieren systems for future researchers.

2.1. Modeling compressible flow through a micro-orifice

Compressibility of a gas is dependent on Mach number. Flow can be generically defined as incompressible when the Mach number is much less than one (White, 2008). If the Mach number of a flow is more than 0.3, flow can be assumed to be compressible (White, 2008; Saad, 1985).

The maximum or choked mass flow rate for compressible flow through a micro-orifice is defined as (White, 2008):

$$\dot{m} = \rho^* A^* V^* = C_D A P_0 \sqrt{\frac{\gamma}{R T_0} \left(\frac{2}{1+\gamma}\right)^{(\gamma+1)/(\gamma-1)}} \tag{1}$$

where ρ^* is the critical density in kg/m³, A^* is the critical area in m², V^* is the critical free stream velocity in m/s, C_D is the discharge coefficient, R is the specific gas constant in m²/(s² K), P_0 is the absolute stagnation pressure in Pa, T_0 is the stagnation temperature in K, and γ is the specific heat ratio. Orifice mass flow rates when flow is not choked can be modeled by:

$$\dot{m} = C_D A P_0 \sqrt{\frac{1}{RT_0} \left(\frac{2\gamma}{1-\gamma}\right) \left(\frac{P}{P_0}\right)^{\frac{2}{\gamma}} \left(1 - \frac{P}{P_0}^{\frac{\gamma-1}{\gamma}}\right)}$$
 (2)

where P is the absolute downstream pressure. The discharge coefficient,

$$C_D = \frac{\dot{m}_{\text{exp}}}{\dot{m}_{\text{isen}}} \tag{3}$$

for a given micro-orifice is defined by the relation of the measured flow rate, $\dot{m}_{\rm exp}$, to the isentropic flow rate, $\dot{m}_{\rm isen}$. Isentropic or lossless flow is defined as having $C_D=1$.

2.2. Schlieren imaging theory

Disturbances in gaseous media can be identified by slight changes in refractive index. Schlieren imaging leverages a relationship between the refractive index and the density of a transparent working fluid. For gases, this relationship is defined by:

$$n - 1 = \kappa \rho \tag{4}$$

where n is the refractive index and κ is the Gladstone–Dale coefficient. The refractive index, $n=c_0/c$, is a description of the speed of light in a vacuum, c_0 , relative to the speed of light moving through the fluid, c. For compressible fluids such as air, changes in density due to changes in temperature or pressure lead to a slight shift in the refractive index:

$$\frac{c_0}{c} - 1 = \kappa \frac{P}{RT} \tag{5}$$

In schlieren imaging, the central objective is to analyze the refraction of light rays. The theory used for light refraction in schlieren objects is a simplification of more complex optical phenomena as described by Settles (2001). For the study of shock structures created by micro-orifice jetting profiles, the simplifications are satisfactory (Kleine, 2001). An example of a two lens Toepler's schlieren apparatus using an extended light source is later described in Fig. 3.

In a two lens schlieren system, it is beneficial to optimize for illuminance, contrast, and sensitivity. Image sensor noise reduction can be achieved by maximizing the illuminance incident on the collimating lens, L_1 :

$$E = \frac{\pi B d_s^2}{4f_1^2} \tag{6}$$

where B is the luminance emitted by the light source, d_s is the diameter of the light source and f_1 is the focal length of L_1 . Increasing the difference in illuminance between the background and the studied object, or image contrast as defined by:

$$C = \frac{\Delta E}{E} = \frac{f_2 \epsilon_y}{h} \tag{7}$$

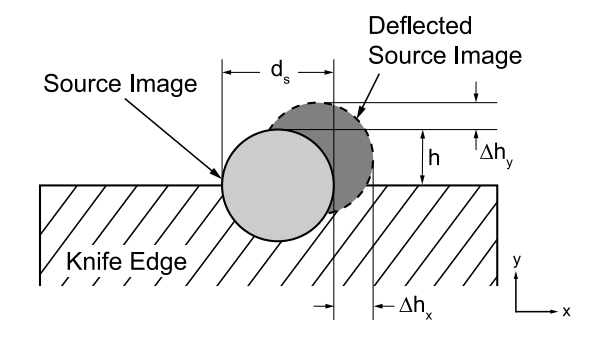


Fig. 1. A schematic of a knife edge cutoff displaying the variables of note relative to the incoming light, and the light that passes by the cutoff.

where f_2 is the focal length of the schlieren lens increases the ability of the system to measure changes in n. Sensitivity of a schlieren system:

$$S = \frac{dC}{ds} = \frac{f_2}{h} \tag{8}$$

where h is the height of the source image extending above the cutoff as shown in Fig. 1 defines the minimum change in n that results in a measurable change in contrast.

The cutoff location within the XY plane defines h and is critical to system performance. An example of a cutoff is shown in Fig. 1. Here, Δh_x is the shift of the source image in the x direction, and Δh_y is the shift of the source image in the y direction. Δh_x and Δh_y can be used to quantify ϵ as in:

$$\epsilon_y = \frac{\Delta h_y}{f_2} \tag{9}$$

Following (8), it is evident that the sensitivity of a schlieren system can be increased by either increasing the focal length of the schlieren lens or by reducing size of the source light spot. There are practical limits to both the aforementioned efforts. For example, increasing f_2 will make it more difficult to visualize small objects; while reducing d_s has potential to increase noise at the image sensor and also to introduce diffractive noise from the cutoff in the captured image.

3. Methods

Circular micro-orifice flow was characterized using three methods. The primary method of characterization used experimental flow rate testing. In this method, the micro-orifices were studied using a test stand for characterization of component flow rate performance. During flow rate testing, the shock structures created at the outlet of the micro-orifices were analyzed using a two lens schlieren system. Lastly, two dimensional axisymmetric numerical turbulence models were used to replicate experimental flow testing conditions. The numerical models were used to study both flow rate and exit flow field.

The following section will start with describing the experimental methods and test benches used to characterize each of the three objectives. Then, the manufacturing methods for creating the microorifice samples will be described. Lastly, the numerical domain and environment will be defined.

3.1. Experimental flow rate test bench

The experimental flow rate characterization test bench consists of a series of sensors and a micro-orifice array test bed as shown in Fig. 2. This test bench is based on an ISO standardized test bench with the modifications being: two quick disconnect fittings connecting a pneumatic line from the upstream pressure and temperature measuring tube to the micro-orifice test bed, and an additional stagnation pressure sensor in the micro-orifice array test bed (Anon, 1989). The sensors

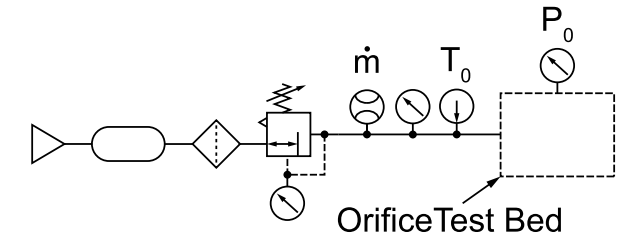


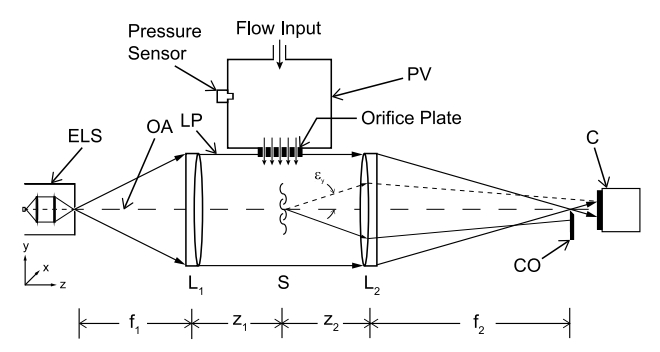
Fig. 2. The flow rate test stand with sensors outputting mass flow rate (m), stagnation pressure (P_0) , and stagnation temperature (T_0) shown alongside the micro-orifice test bed

used in the test bench include: an upstream temperature sensor to measure stagnation temperature, T_0 , of the source gas, an upstream pressure sensor to measure in line stagnation pressure, a mass flow meter to measure mass flow rate, \dot{m} , and a downstream pressure sensor to measure the stagnation pressure, P_0 , in the pressure vessel. Note that all flow rates were measured venting to atmospheric pressure. Atmospheric pressure was assumed to be 101,325 Pa. The measured parameters from this test bench in conjunction with accurate measurement of micro-orifice dimensions allowed for complete characterization of the flow rate performance of the orifice plate designs tested.

3.2. Schlieren test bench

The schlieren setup used to characterize the microjets exiting the micro-orifices is generally described in Section 2.2 as a two lens Toepler's type schlieren system. The schematic of the system used in testing is described by Fig. 3. The use of a two lens system as opposed to more complicated setups allowed for a compact test bench with cost effective components.

The system consisted of a custom extended light source (ELS), two lenses (L_1 and L_2), a pressure vessel (PV) that acted as a test bed for mounting different orifice plate designs, a light cutoff (CO), an imaging lens assembly, and a camera (C). Here an orifice plate is defined as



(a) Schematic of the two lens schlieren system used to analyze the microorifice jetting profile.

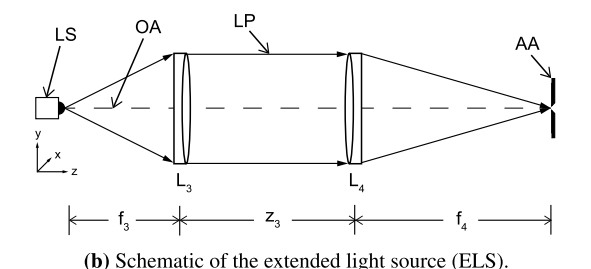


Fig. 3. Description of schlieren system used to analyze micro-orifice jetting profile.

the test workpiece containing an array of micro-orifices. The ELS used a 635 lumen 5 W white LED light source (LS) with a 5000 K color temperature. This LED was mounted to a cage using a paired set of one inch achromatic doublet lenses, L_3 and L_4 . The focal lengths for L_3 and L_4 , f_3 and f_4 respectively, were 50 mm. The paired doublet lenses were used to collimate and re-focus the light emitted from the LED onto a 700 μm pinhole (AA). Light exiting the pinhole acted as the light source for the schlieren system.

A two inch diameter achromatic doublet lens was used for L_1 with a focal length, f_1 , of 200 mm. A matched lens was chosen for L_2 so that the focal lengths of L_1 and L_2 were equal, $f_1=f_2$, and d_s maintained the pinhole diameter of 700 μ m. The distance for the spacing between the lenses, z_1+z_2 , was determined by:

$$z_1 = f_4 + f_1 \tag{10}$$

and

$$z_2 = 2f_2 \tag{11}$$

 ${\bf L}_2$ focused the light onto the cutoff. In this study, the cutoff used was a horizontal knife edge. 1

The imaging lens assembly used after the cutoff was chosen to minimize working distance while maintaining a sufficiently high focal length to visualize microscale objects. The assembly paired a variable zoom lens with focal lengths ranging from 35 mm to 150 mm, with a 2x telefocal extender and a 50 mm long lens tube. The effective 300 mm focal length of the lens assembly, combined with the lens tube and z_2 defined by (11) allowed for an average object magnification of 2.4x.

The camera used for the imaging was a Nikon D780. This was chosen for the sensor quality, as well as for the pixel count to allow for post processing image cropping without a degradation in image resolution. The resulting system used is shown in Fig. 4. Two axis positioners were used to align the ELS with L_1 , and then also to position the cutoff. A three axis gimbal mount was used to position the imaging camera and lens assembly.

3.3. Orifice plate manufacturing

A central goal of the study is to determine the impact of using multiple circular micro-orifices versus a single macroscale circular orifice in a pneumatic system. As such, a variety of orifice plate designs were manufactured and tested as described in Table 1. Table 1 column header parameters d_1 , d_2 , and X_2 are shown in Fig. 5. In Fig. 5 the following dimensions are parametrically defined: X_1 is the length of the upstream fluid domain, X_2 is the orifice plate thickness, X_3 is the length of the downstream fluid domain, d_1 is the minimum micro-orifice diameter, d_2 is the maximum micro-orifice diameter, and d_3 is the fluid domain diameter. The manufactured orifice plates can be broken down into three populations.

The first population, orifice plate designs 1 through 5, was designed to determine the impacts of discretizing a single circular large orifice into an array of smaller circular micro-orifices with summative equivalent area. These micro-orifices were drilled and reamed to ensure the geometry could be well defined, and serve as a control for populations two and three. A 1 mm diameter was chosen for the primary orifice plate design to maintain scale relevance to orifices used in fluid handling and control applications. A schematic for this population is shown in Fig. 5a.

The second population, orifice plate designs 6 through 9, consisted of a set of etched silicon circular micro-orifice arrays. These orifice plate designs mimic the intent from the first population. The silicon

¹ It is recognized that more complex cutoffs have been successfully implemented (Settles and Hargather, 2017). However, they were not required to visualize the shock structures present in the microjets at the exit of the micro-orifices.

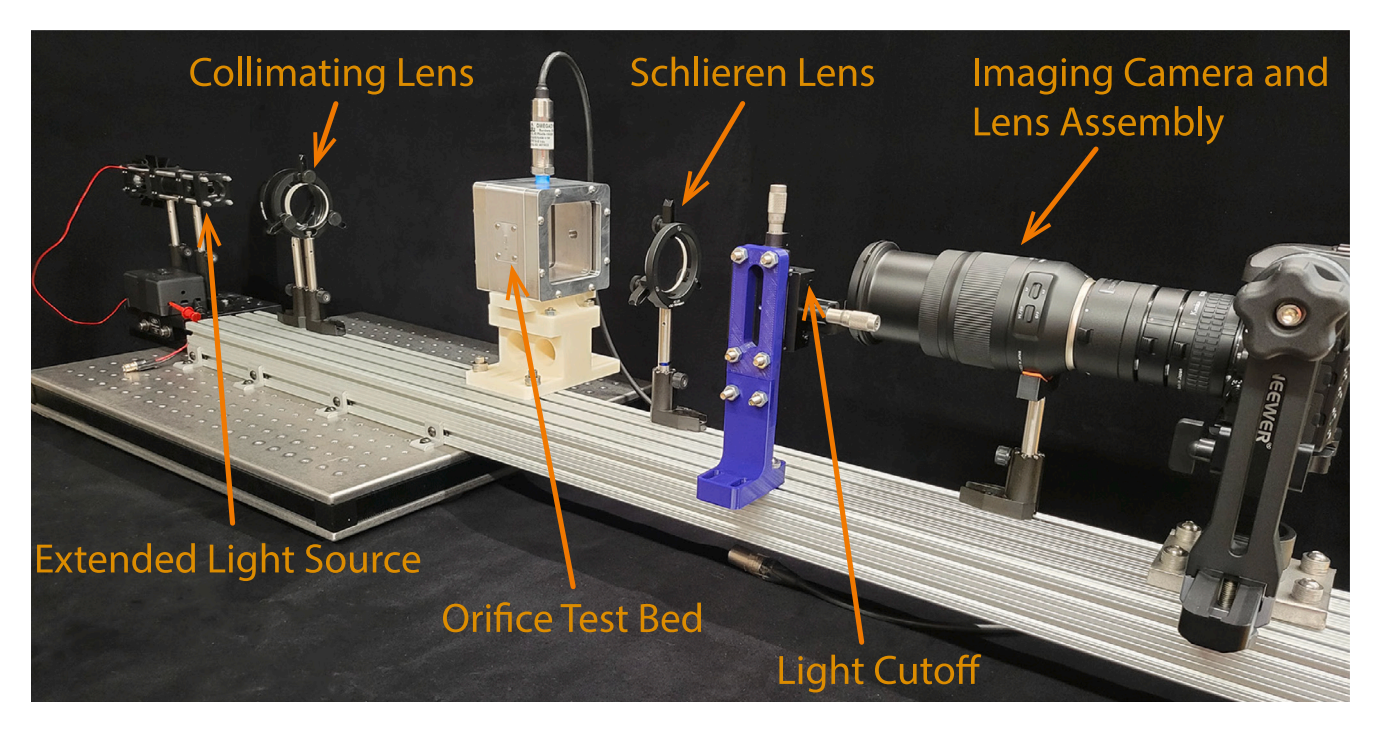
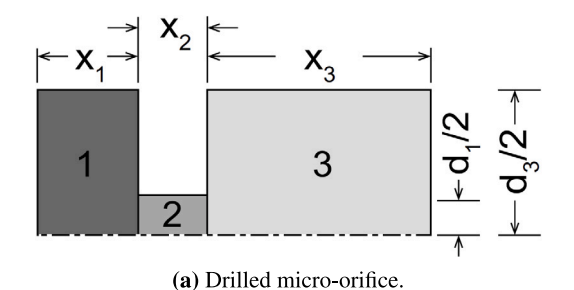


Fig. 4. Two lens schlieren system with an extended light source, a pressure vessel to act as the micro-orifice test bed, and the imaging lens assembly attached the to the Nikon D780.



(b) Etched silicon micro-orifice.

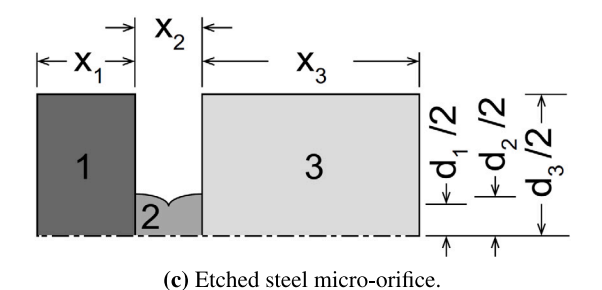


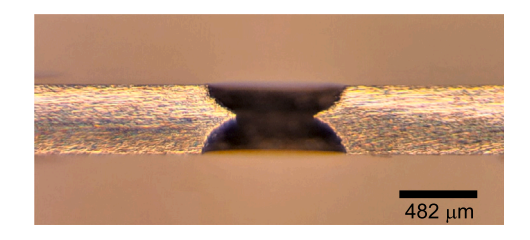
Fig. 5. Parameterized description of axisymmetric micro-orifice geometric domains.

Table 1
Description of micro-orifice array designs tested where D correlates to drilled aluminum orifices, Si correlates to etched silicon micro-orifices, and SS correlates to stainless steel etched micro-orifices.

Orifice plate	Type	d_1	\mathbf{d}_2	\mathbf{X}_2	Taper	N
design		(µm)	(µm)	(µm)	(°)	
1	D	975	N/A	3175	N/A	1
2	D	704	N/A	3175	N/A	2
3	D	504	N/A	3175	N/A	4
4	D	393	N/A	3175	N/A	6
5	D	346	N/A	3175	N/A	8
6	Si	1036	1136	525	5.4	1
7	Si	259	280	525	1.1	16
8	Si	178	185	525	0.4	32
9	Si	132	192	525	3.3	64
10	SS	492	850	393	N/A	1
11	SS	492	850	393	N/A	2
12	SS	492	850	393	N/A	3
13	SS	492	850	393	N/A	4

micro-orifice arrays were etched using a Bosch DRIE process in the same manner as described in Hagstrom et al. (2019). As such, the micro-orifice side walls can be thought of as nominally anisotropic. However, it is possible for the etching to contribute as much as a 5 degree micro-orifice wall taper creating a difference between inlet and outlet diameters (Chang et al., 2018; Tang et al., 2017). Taper angles from 0.4° to 5.4° were observed in this population as shown in Table 1. A micro-orifice schematic for this population is shown in Fig. 5b.

The third and final population, orifice plate design 10 through 13, consisted of a set of etched stainless steel micro-orifice arrays. The etched steel circular micro-orifices were created using a photochemical etching (PCE) operation. This operation uses a dry film as a photomask and a chemical etchant to remove material. The chemical etchant undercuts the edges of the photomask pattern resulting in scallop shapes at the substrate surfaces. The micro-orifice wall profile used in numerical modeling is shown in 5c. A cross-section of a representative photochemically etched micro-orifice is shown in Fig. 6 to illustrate the actual wall profile. The intent for the third population was to determine the impacts of increasing the number of equally sized micro-orifices on flow capacity.



 $\textbf{Fig. 6.} \ \ \text{Cross-section to illustrate wall profile for orifice plate designs} \ \ 10$

 Table 2

 Geometric parameters of numerically modeled micro-orifice designs.

Orifice design	X ₁ (μm)	X ₂ (μm)	X ₃ (μm)	d ₁ (μm)	d ₂ (μm)	d ₃ (μm)
1	2000	3175	10000	1000	N/A	6000
2	2000	3175	10000	700	N/A	6000
3	2000	3175	10000	500	N/A	6000
4	2000	3175	10000	400	N/A	6000
5	2000	3175	10000	350	N/A	6000
6	2000	525	10000	1036	1136	5000
7	500	525	2500	259	280	1250
8	370	525	1850	178	185	925
9	370	525	1850	132	191.6	925
10–13	3000	528	10000	492	850	7000

The diametric dimensions described in Table 1 were gathered from optical measurements. For the orifice plates with more than one micro-orifice, the dimensions defined in Table 1 reflect an average of all micro-orifices measured. Orifice plate designs 1 though 5, and 10 through 13 were measured using an optical system accurate to within $\pm 5.4~\mu m$. The optical system to measure the silicon micro-orifices was accurate to within $\pm 2~\mu m$. The optical systems enabled accurate in plane measurements. Depth or profile type measurements were not reliable with the optical systems used. As such, creation of the concave features shown in Fig. 5c for the numerical domain of orifice plate designs 10 through 13 were created from the two measured diameters and from comparison with the sample cross-section illustrated by Fig. 6.

3.4. Numerical domain

The numerical domains were implemented using ANSYS Fluent Academic Research Version 20.2. Micro-orifice flow was modeled in a two dimensional axisymmetric domain with a steady state pressure based solver. The solver used second order spatial discretization with a coupled pressure–velocity scheme. The SST transition turbulence viscous model was used as described by Menter et al. (2006) in conjunction with the energy equation. The geometry for each of the drilled, silicon etched, and steel etched micro-orifices are described by Fig. 5 with dimensions specified in Table 2. Ten discrete domains were created.

The SST transition model was used as it is able to accurately simulate the shock structure of a supersonic free jet (Evgenevna et al., 2014). The SST transition model is able to do this as it applies the $k-\omega$ turbulence model near the boundary layer, with the $k-\varepsilon$ model in the free field. The SST transition model builds upon the $k-\omega$ SST model by adding two transport equations to better model the transition between laminar and turbulent flow.

The Transition SST model requires a fine mesh at the walls. The metric used for grid sizing at the walls is the dimensionless wall distance:

$$y^{+} = \frac{yu_{\tau}}{y} \tag{12}$$

where y is the distance to the wall, v is the kinematic viscosity, and u_{τ} is the shear velocity. Shear velocity is defined by:

$$u_{\tau} = \sqrt{\frac{\tau}{\rho}} \tag{13}$$

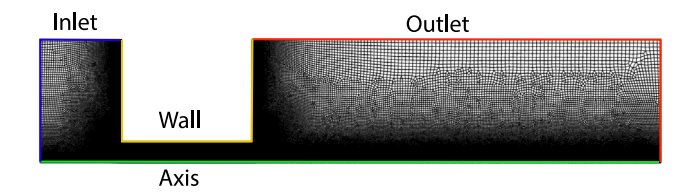


Fig. 7. Representative mesh for orifice plate design 1 with inlet boundary condition as blue, the wall as orange, the outlet as red, and the axis as green. (For interpretation of the references to color in this figure legend, the reader is referred to the web version of this article.)

where τ is the shear stress at the wall. Maintaining a $y^+ < 1$ value at the wall allowed for the model to accurately resolve into the viscous sub-layer.

Unstructured grids were used to mesh geometry zones 1, 2, and 3 as described by Fig. 5. Mesh sensitivity studies were performed at 600 kPa gauge inlet pressure for the unstructured grids. For the mesh used with each micro-orifice design, the difference in estimated flow rate varied less than 1% from the previously tested grid with 50% larger cell dimensions. The resulting unstructured grid used a cell sizing of 1 μm along the micro-orifice wall and along the axis for the length of the micro-orifice wall. A 10 μm cell size was specified at the top and bottom wall of the orifice plate. A 5 μm cell size was specified along the axis upstream and downstream from the micro-orifice. Cell growth rate was defined as 1.02. Representative mesh and boundary condition locations are shown in Fig. 7.

The boundary conditions used were as follows. The inlet was set to a pressure inlet with the inlet pressure ranging from 50 kPa gauge to 600 kPa gauge for each of the designs modeled. The wall used a no-slip boundary condition. The outlet was set to a pressure outlet with the pressure at 0 kPa. The atmospheric pressure was set to 101.325 kPa. The axis was used as the axisymmetric boundary condition.

4. Results

The results from the studies described are presented in three subsections. The first subsection describes the results gathered from experimental flow rate characterization. The second subsection describes the data acquired from schlieren imaging. The third subsection describes the results from numerical testing and compares results against experimental flow rate testing and schlieren imaging.

4.1. Experimental flow capacity

Experimental flow rate characterization was conducted for each of the orifice plate designs described by Table 1. Air was used as the working fluid. Here, inlet pressure was varied from 0 kPa to 600 kPa gauge inlet pressure while the outlet was venting to atmospheric pressure. The inlet pressure was limited to 600 kPa gauge as the pressure supply was limited to 600 kPa. The other present limitation was flow meter capacity. The flow meter used had a maximum capacity of 100 SLPM, limiting measurements to 100 SLPM or less.

The first set of orifice plate designs tested, design 1 through 5, were standard drilled micro-orifices. The target equivalent area was $7.854\times10^{-1}~\text{mm}^2$. This correlated to a 1 mm diameter orifice for orifice plate design 1. Orifice plate designs 2, 3, 4, and 5 used micro-orifice arrays with largely equivalent summative areas: $2\times700~\mu\text{m},~4\times500~\mu\text{m},~6\times400~\mu\text{m},~\text{and}~8\times350~\mu\text{m}.$ While not exactly equivalent in area to a singular 1 mm orifice, these designs were used as the diameters corresponded to standard drill sizes. Exact measurements from the orifice plate designs are presented in Table 1.

² Alicat M-Series 100 SLPM capacity mass flow meter.

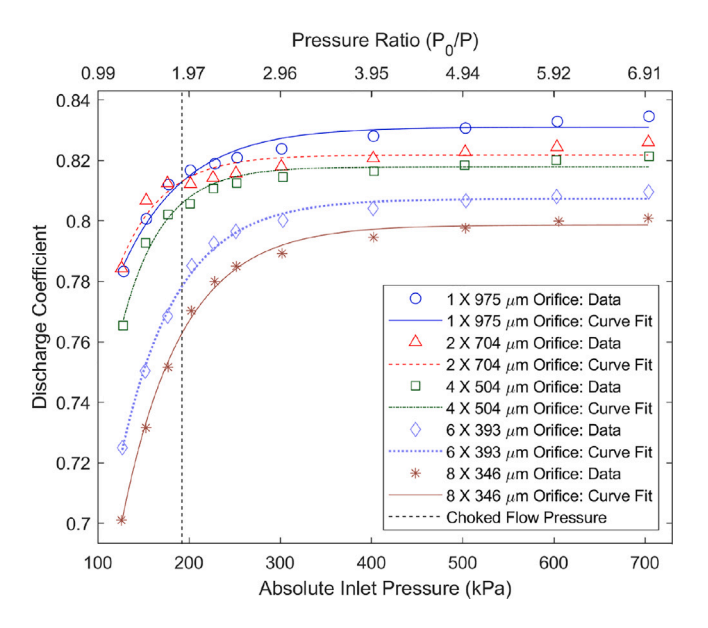


Fig. 8. Plot of C_D versus inlet pressure for drilled orifice plate designs 1 through 5. Data is shown by circles and is fit using (14).

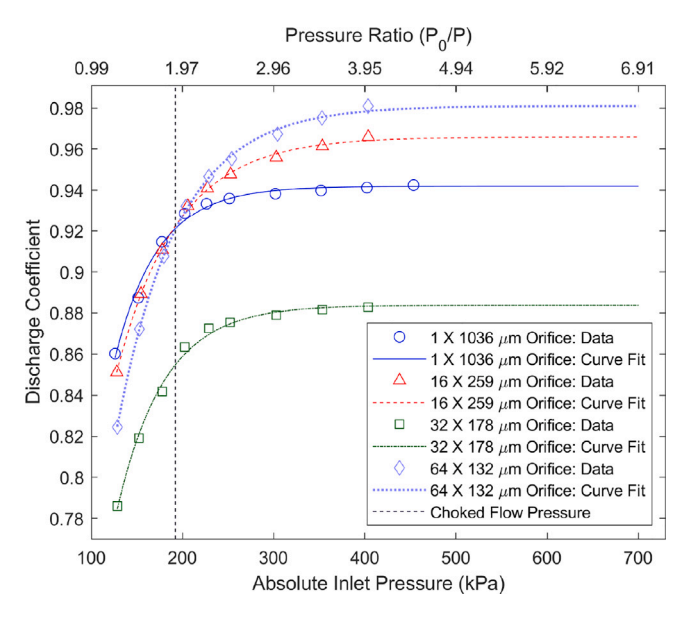


Fig. 9. Plot of C_D versus inlet pressure for etched silicon orifice plate designs 6 through 9. Data is shown by circles and is fit using (14).

As it was not practical to exactly match summative micro-orifice areas, orifice plate designs were compared based on C_D . Here, micro-orifice areas were defined based on measured diameters, d_1 , as defined in Table 1. Studying C_D relative to input pressure allowed for comparison of relative efficiencies for all designs at specific inlet pressures. As the outlet pressure was assumed to be constant and at one atmosphere, the comparison of C_D versus inlet pressure can also be used to infer the relation of C_D to driving pressure difference.

The discharge coefficient for orifice plate designs 1 through 5 is shown in Fig. 8 plotted against both absolute inlet pressure and pressure ratio. Here the experimental data for each design was fit against the form shown:

$$C_D = X_1 - X_2 e^{-X_3(P_0/P)} (14)$$

where X_1 , X_2 , and X_3 are independent fitting parameters. This form was chosen as C_D appeared to have an asymptotic relationship to the

Table 3

Curve fit parameters for drilled orifice plate designs.

Orifice plate design	X_1	X_2	X_3	$\Delta C_{D,max}$
1	0.8310	0.2913	1.4650	0.0458
2	0.8218	0.4881	2.1228	0.0349
3	0.8179	0.8761	2.2608	0.0506
4	0.8073	0.6370	1.6302	0.0830
5	0.7987	0.6724	1.5463	0.0984

Table 4
Curve fit parameters for etched silicon orifice plate designs

our re me purume.	cro for eterree	omicon ormic	prace design	•
Orifice plate design	X_1	X_2	X_3	$\Delta C_{\mathrm{D,max}}$
6	0.9420	1.1883	2.1238	0.0837
7	0.9659	0.7923	1.5302	0.1147
8	0.8839	1.1860	1.9556	0.0992
9	0.9810	1.0663	1.5138	0.1562

pressure ratio. The curve fit results for orifice plate designs 1 through 5 are shown in Table 3.

 X_1 represents the maximum discharge coefficient possible for an orifice plate design. As such, comparison of X_1 allowed for simple comparison of the maximum efficiency for each orifice plate design. As shown in Table 3, there is a significant trend in X_1 related to orifice plate design. The single 975 μ m orifice had a maximum C_D of 0.8310 where as the smallest micro-orifice array with the largest number of orifices had a comparatively smaller C_D of 0.7987. In addition, a significant performance difference existed between the C_D measured at the minimum tested pressure and the C_D measured at the maximum tested pressure. The difference is quantified as $\Delta C_{D,\max}$ as shown in Table 3. For the single orifice design, $\Delta C_{D,\max}$ is 0.0458 and for the eight micro-orifice design $\Delta C_{D,\max}$ is 0.0984.

The second set of orifice plate designs correspond to designs 6 through 9 as defined by Table 1. These designs were sized such that each design had an equivalent summative area. The experimentally measured C_D versus absolute inlet pressure and pressure ratio are shown in Fig. 9. The four silicon etched orifice plates had different maximum X_1 as well as different $\Delta C_{D,\max}$ as represented by the curve fit results shown in Table 4. With these designs, there was not a trend related to the number or size of micro-orifices used. The 64 micro-orifice design had the highest X_1 of 0.9810 and the highest $\Delta C_{D,\max}$ of 0.1562.

The last set of orifice plate designs tested were the etched stainless steel micro-orifices. The results from this testing are shown in Fig. 10. Orifice plate designs 10 through 13 correspond to orifice plates using an incrementally increasing number of micro-orifices of the same diameter and aspect ratio, d_1/X_2 . This corresponded to testing $1\times492~\mu m$, $2\times492~\mu m$, $3\times492~\mu m$, and $4\times492~\mu m$ micro-orifices. This testing investigated the trend between added number of micro-orifices and any change in flow capacity.

The values of X_1 for the etched stainless steel micro-orifice arrays were close to unity. The four orifice plate designs tested performed similarly with maximum C_D and $\Delta C_{D,\max}$ showing little variation. This signifies that for the tested orifice plate designs, there was a linear relationship between added micro-orifices and a corresponding increase in flow capacity. The curve fit parameters for the stainless steel etched orifice plate designs are shown in Table 5.

Measurement uncertainty of the experimentally measured C_D data is defined as E_{C_D} . E_{C_D} was attributed to two factors. The first factor contributing to E_{C_D} was the flow meter measurement uncertainty defined as:

$$E_{\dot{m}, \text{exp}} = \pm (2.00 \times 10^{-3} + 4.00 \times 10^{-3} (\dot{m}_{\text{exp}}))$$
 (15)

in units of g/s where $\dot{m}_{\rm exp}$ is the measured mass flow rate. The second factor was error in predicted mass flow rate due to accuracy limitations

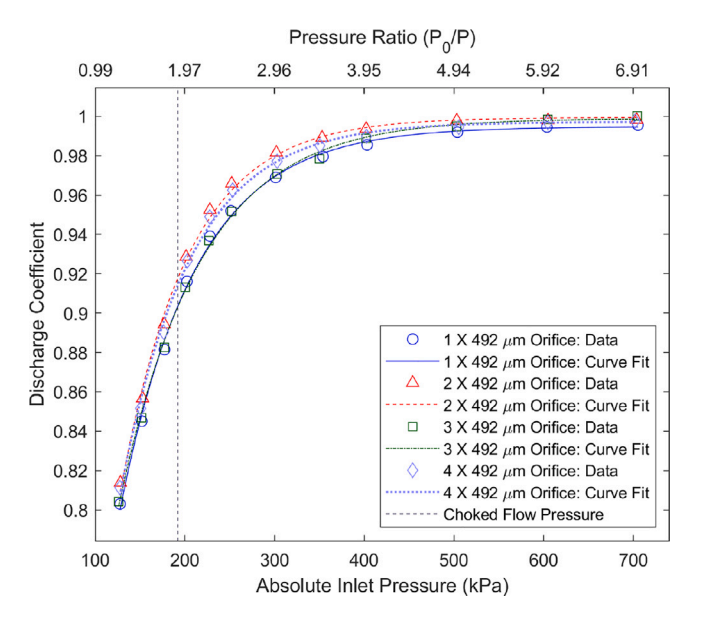


Fig. 10. Plot of C_D versus inlet pressure for etched stainless steel orifice plate designs 10 through 13. Data is shown by circles and is fit using (14).

Table 5
Curve fit parameters for etched steel orifice plate designs.

Orifice plate design	X_1	\mathbf{X}_2	X_3	$\Delta C_{D,max}$
10	0.9948	0.8778	1.1947	0.1945
11	0.9994	1.0327	1.3381	0.1900
12	0.9990	0.7876	1.1116	0.1964
13	0.9972	0.9768	1.3002	0.1897

in micro-orifice diameter measurement. This factor is asymmetric and defined as:

$$E_{\dot{m},\rm isen} = \left(\frac{\dot{m}}{D^2}\right) (D \pm D_{\rm error})^2 \tag{16}$$

where D_{error} is the micro-orifice measurement accuracy. E_{C_D} is the ratio of (15) to (16) in following (3). Sample error bars for $E_{\dot{m},\mathrm{exp}}$ and E_{C_D} are shown in Fig. 17 and Fig. 18 respectively.

4.2. Schlieren imaging

Schlieren analysis was conducted for orifice plate designs 1 through 5 to characterize microjet profiles at the exit of the micro-orifice arrays. Analysis of orifice plate designs 6 through 13 was not possible as the fixturing required to allow for microjet visualization made the orifice plate susceptible to yielding or fracture. The process of image analysis and post processing will be described followed by presentation of the images taken and data extracted.

The schlieren lens used in the system was selected due to focal length and surface quality. However, after taking a few images it became apparent that the thickness of the lens added noise to the schlieren image. Fig. 11a represents the cropped unedited version of a schlieren image when testing orifice plate design 1. Fig. 11b represents the same schlieren image with background subtraction alongside contrast stretching to aid in the ability to visualize weak schlieren objects.

Background image subtraction worked as follows. A representative image was taken with pressure at 0 kPa with no flow moving through the orifices. When images were taken at increased inlet pressures, this background image could act as a mask to remove noise associated with the lens and any other steady state contributors of image noise. An example of the results using this method for orifice plate designs 1 through 5 are shown in Fig. 12 for flow at 400 kPa gauge inlet pressure.



(a) Schlieren image of orifice jetting profile.



(b) Schlieren image of orifice jetting profile with background subtraction.

Fig. 11. Schlieren image of 975 μm orifice jetting profile at 400 kPa gauge.

Schlieren images were taken at the following pressures: 50, 100, 150, 200, 300, 400, 500, and 600 kPa gauge inlet pressure for orifice plate designs 1 through 5. For the sake of comparison between orifice plate designs, images from tests conducted at 400 kPa were presented as each design displayed well defined shock structures. Fig. 12 illustrates schlieren images³ from orifice plate designs 1 through 5 respectively.

As evident in each design, flow at the exit of the orifices at 400 kPa exhibited an underexpanded supersonic jet. In each of orifice plate designs 1 through 5 the shock cells, reflected oblique shocks, and jet boundaries were clearly visible. For purposes of quantitative comparison between numerical results and the schlieren imaging results, the shock cell spacing was measured. Pixel value measurements were gathered using a line measurement of data offset from the jet centerline as shown in Fig. 13. The measurement line was offset from the jet centerline as larger gradients in pixel values occurred closer to the jet boundaries due to use of a horizontal knife edge type cutoff in the schlieren system. This resulted in better measurement of shock cell spacing. The color gradient in the schlieren images where the top of the jet boundary is dark and the bottom of the jet boundary is light is due to the use of a horizontal cutoff.

The pixel value measurements for orifice plate designs 1 through 5 are shown in Fig. 14. The measured spacing from the first shock cell to the second shock cell is shown in Table 6 with respect to orifice plate design and orifice diameter. The line measurement data displayed a clear relationship between orifice aspect ratio, orifice diameter, and first shock cell spacing. The data suggested that decreasing the orifice diameter led to a decreased shock cell spacing and a corresponding decrease in distance for the jet velocity to reduce to ambient conditions.

4.3. Numerical model comparison with schlieren imaging

The numerically modeled density fields for the orifice plate designs were plotted to capture the shock cell structure as well as to compare

 $^{^3}$ Note that observed jet deflections in Fig. 12b, 12c, and 12e are artifacts of orifice plate manufacturing.

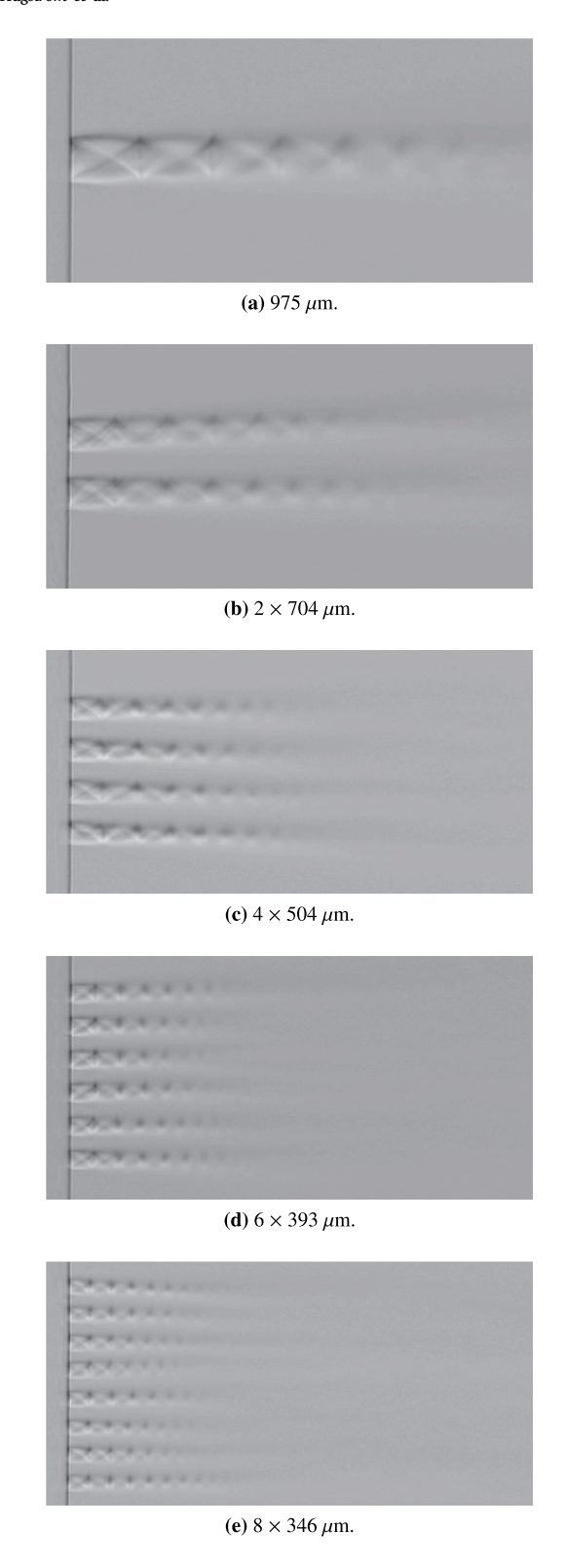


Fig. 12. Schlieren images of the jetting profiles of drilled orifice plate designs at $400\ \text{kPa}$ gauge inlet pressure venting to atmosphere.

against schlieren imaging. As 400 kPa gauge was used as the inlet pressure for comparison of experimentally visualized shock structures, the same pressure was also used for the numerical models. Modeled density contours for orifice plate design 5 are shown in Fig. 15. The density contours clearly show the shock cell structure and jet boundary.

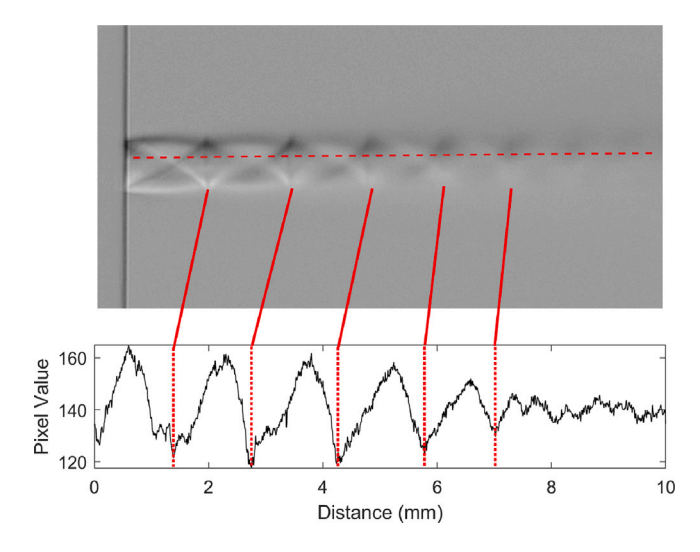


Fig. 13. 975 μ m orifice jetting at 400 kPa gauge inlet pressure with pixel values plotted versus distance. The pixel value plot allows for quantitative measurement of shock cell period, the distance between each of the red lines.

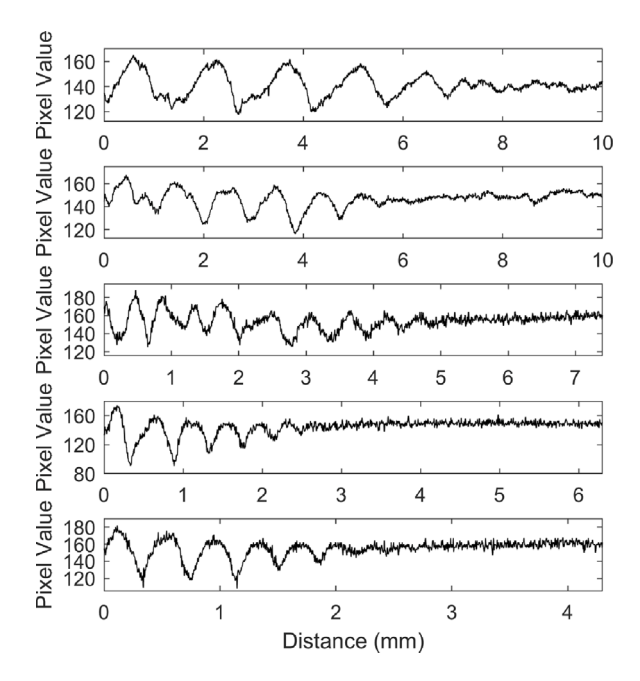


Fig. 14. Measured centerline pixel value for the 975 μm orifice (1st), 704 μm micro-orifice (2nd), 504 μm micro-orifice (3rd), 393 μm micro-orifice (4th), and the 346 μm micro-orifice (5th) at 400 kPa gauge.

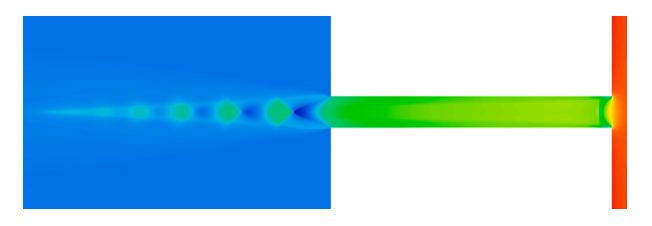
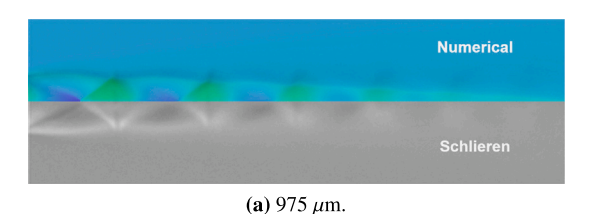


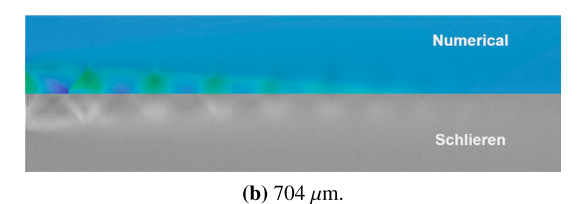
Fig. 15. $350 \mu m$ micro-orifice jetting at 400 kPa. (For interpretation of the references to color in this figure legend, the reader is referred to the web version of this article.)

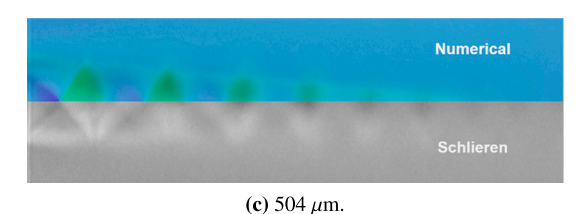
Density contours were chosen as the output of the numerical models as changes in density are proportional to changes in refractive index as described by (5) when using air. As such, the schlieren objects visualized and the numerical model output should be equivalent. The

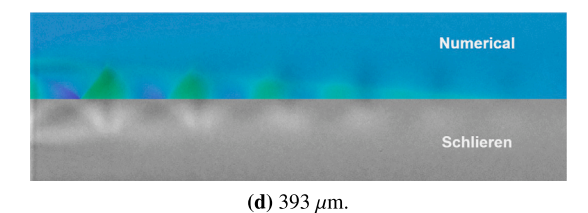
Table 6
First shock cell spacing data gathered from orifice plate designs 1 through 5 using the schlieren method.

Orifice plate	Orifice	Schlieren	Numerical
design	diameter	shock cell	shock cell
		spacing	spacing
	(µm)	(µm)	(µm)
1	975	1344	1537
2	704	981	1010
3	504	750	771
4	393	547	619
5	346	419	533









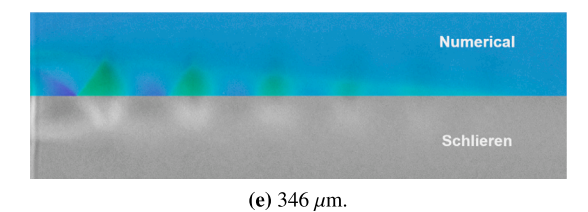


Fig. 16. Comparison between numerical solution and schlieren images of the jetting profiles for orifice plate designs 1 through 5. (For interpretation of the references to color in this figure legend, the reader is referred to the web version of this article.)

shock cell structures captured by schlieren and numerical modeling were compared for orifice plate designs 1 through 5 as shown in Fig. 16. It is of note that the measured orifice plate dimensions showed slight geometric variance from the computational geometric domain. The variance can be seen when comparing d_1 and d_2 values from Table 1 and d_1 and d_2 from Table 2 respectively.

Numerical solutions are shown in color on the top half of the subfigure image, and schlieren images are shown in greyscale on the bottom half of the subfigure image as seen in Fig. 16a through 16e. For orifice plate designs 2 through 5, a single microjet was compared against the numerical solution. The magnitude of the density was not defined in Fig. 16 as the object of interest was spatial comparison of shock structures. As seen in Fig. 16, the numerical models were able to closely replicate the shock structures seen in schlieren imaging.

4.4. Numerical model comparison with flow rate testing

Mass flow rate data was extracted from each orifice plate design numerical model. This data was plotted in comparison to mass flow rate data gathered experimentally as well as against the theoretical lossless mass flow rate. The flow rate comparison for the $8\times346~\mu m$ micro-orifice array (design 5) is shown in Fig. 17. Differences in flow rate data between numerical model and experimental data can be accounted for by differences in orifice dimensions. The orifice diameters in the numerical domain were sized nominally, where as the measured diameters of the tested orifice plate designs varied from the nominal value. For this reason, C_D was used as the metric for comparison of performance between numerical and experimental domains. Such a comparison is shown in Fig. 18 for the $8 \times 346 \mu m$ micro-orifice array. The equivalent area for the micro-orifice arrays used to calculate C_D was defined from the summed area of each individual micro-orifice. As numerical models were completed in an axisymmetric domain, the flow rate data for orifice plates having more than one orifice were determined by multiplying the single-orifice flow rate by the number of orifices; e.g., it was assumed that flows from adjacent orifices did not interact.

Comparison of experimental discharge coefficients and numerical discharge coefficients showed similar values and trends. The differences between experimentally determined C_D and numerically determined C_D for orifice plate designs 1 through 5 are shown in Fig. 19. The differences between experimental and numerical values decreased with increasing pressure and flow rate. Here orifice plate designs tested at sonic conditions showed the lowest percent difference with values as low as 0.5% for designs 2 through 5. Orifice plate design 1 slightly deviated from this behavior.

Discharge coefficients were also compared for the silicon etched micro-orifices, orifice plate designs 6 through 9. The comparison between numerical and experimental C_D is shown in Fig. 20. The percent difference followed a similar trend compared with the drilled orifice plate designs with sub-sonic numerical model and experimental values showing the largest percent difference.

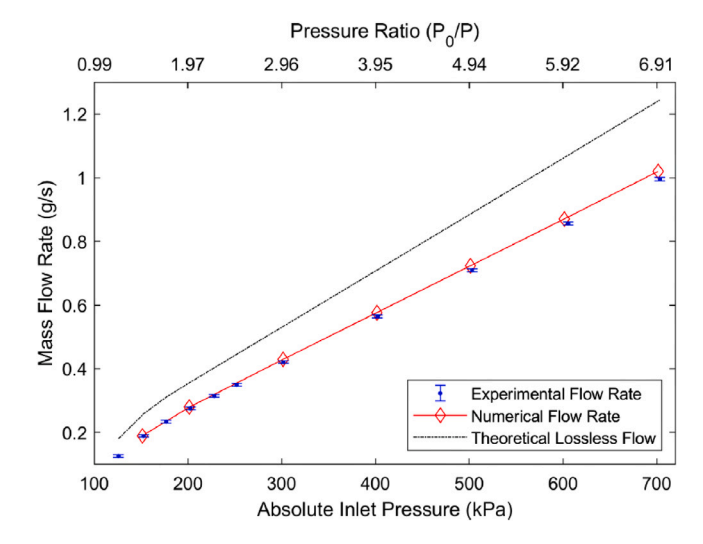


Fig. 17. Mass flow rate measurements for 8 \times 346 μm micro-orifices compared to numerical modeling and theory.

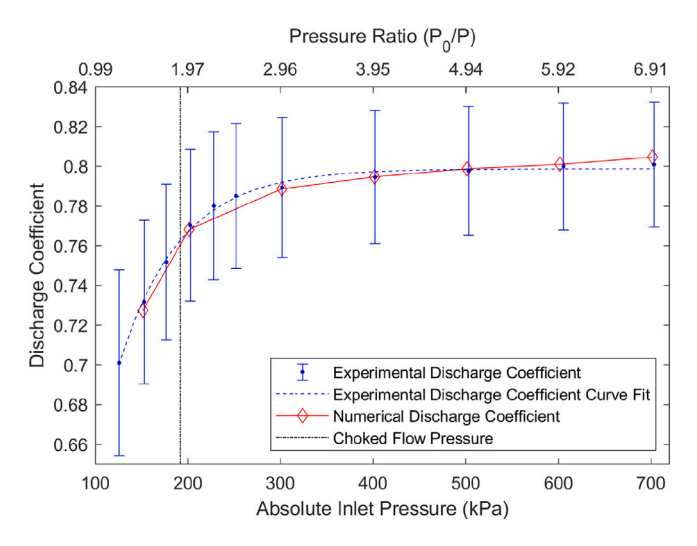


Fig. 18. Experimentally measured discharge coefficients compared to numerically calculated discharge coefficients for $8\times346~\mu m$ micro-orifices.

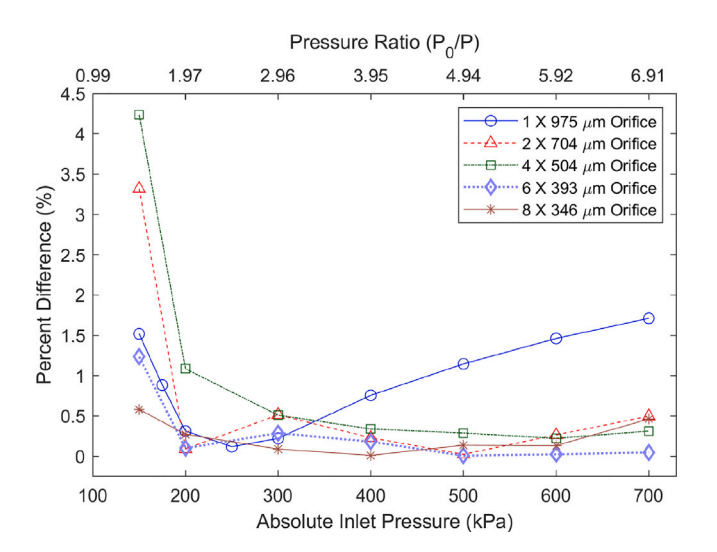


Fig. 19. Percent difference between experimental and numerically calculated C_D for orifice plate designs 1 through 5.

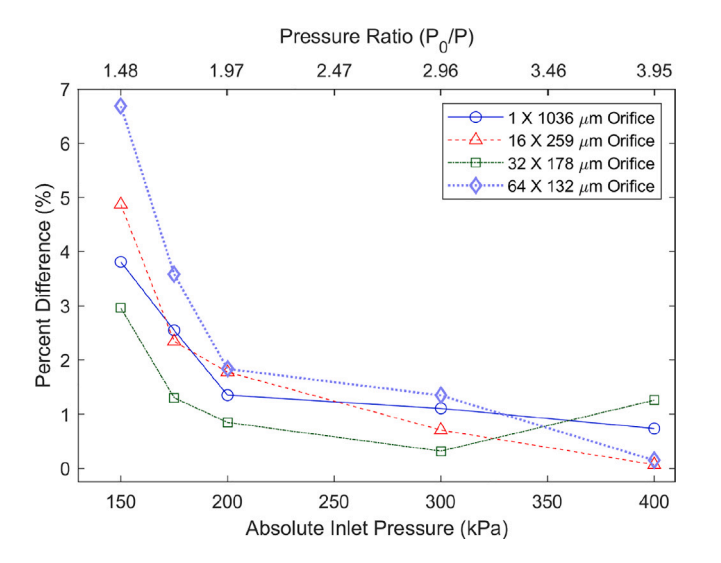


Fig. 20. Percent difference between experimental and numerically calculated C_D for orifice plate designs 6 through 9.

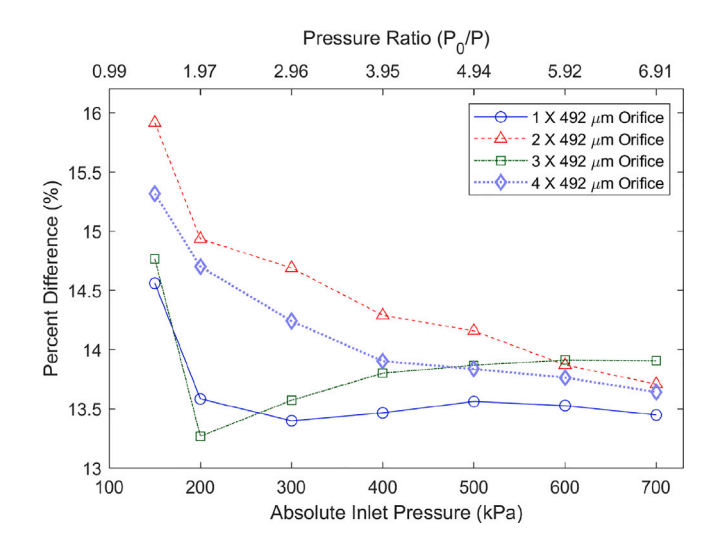


Fig. 21. Percent difference between experimental and numerically calculated C_D for orifice plate designs 10 through 13.

The last comparison between experimental C_D and numerical C_D was with the steel etched micro-orifices, orifice plate designs 10 through 13. The results of the comparison are shown in Fig. 21. The steel etched models showed the largest difference between the numerical models and the experimental data. Here the same trend in percent difference relative to flow rate and inlet pressure was seen as compared to the previous orifice plate designs.

The larger magnitude of percent difference between numerical and experimental data for the etched steel orifice plate designs is likely attributed to variances between the fabricated component micro-orifice wall profile and the modeled micro-orifice geometry used in the numerical models. As shown in Figs. 6 and 5c, the micro-orifice wall profile resembles a converging-diverging nozzle. As such it is recognized that accurate definition of the micro-orifice wall profile is critical to the accuracy of the numerical C_D .

5. Discussion

The experiments completed serve as a reference for understanding how use of micro-orifice arrays impact the flow capacity of pneumatic systems working at larger than microscale transport rates. One area of interest where this knowledge is useful is with flat seat type pneumatic valves. In such valves, the diameter of the orifice serves as a proportional control for the stroke required by the actuator to achieve full flow capacity as previously described by Hagstrom et al. where $\delta_{\text{max}} = D/4$ (Hagstrom et al., 2019). In this type of valve, use of an array of micro-orifices has potential to reduce the actuator stroke required to utilize the full range of seat controlled flow. This stroke reduction would allow use of direct acting actuators with microscale displacement in systems that operate at flow rates of 80 SLPM or even greater. The evidence provided by this work shows that marginal losses in flow capacity may be realized when using a micro-orifice array to replace a single larger orifice. However, the benefits of reducing actuator stroke outweigh the marginal loss in capacity.

The experimental body of evidence as described in Section 4.1 showed that for the drilled orifice plate designs, there was an incremental reduction in C_D moving from design 1 to design 5. This reduction in C_D could be correlated to the increase in number of orifices, the reduction in d_1 , or the corresponding reduction in d_1/X_2 . In Section 4.4 the numerically calculated C_D matched experimental measurements within 3%, suggesting the number of micro-orifices was not a significant factor in reducing C_D .

Jankowski et al. and Hasegawa et al. assert that in short tube orifices, $d_1/X_2 < 0.5$, C_D is dependent on d_1/X_2 where a reduction in

 d_1/X_2 results in a reduction in C_D (Jankowski et al., 2008; Hasegawa et al., 1997). While the work by Jankowski et al. and Hasegawa et al. applies to incompressible flow, Ho and Tai assert that while fluid compressibility and rarefaction effects present in compressible flow affect the linearity or relationship between d_1/X_2 and C_D , the relationship between d_1/X_2 and C_D remains (Ho and Tai, 1998). As orifice designs 1 through 5 are classified as short tube orifices, it is believed that a reduction in d_1/X_2 from design 1 to design 5 is responsible for the reduction in C_D .

When looking at the results for the etched stainless steel orifice plates, orifice plate designs 10 through 13, it can be concluded that increasing the number of micro-orifices should have minimal impact on C_D . This is supported as there was negligible difference in C_D in relation to the number of micro-orifices. Similarly, data for the silicon orifice plates, orifice plate designs 6 through 9, also showed indifference when the number of micro-orifices used is compared against C_D .

It is noted that C_D results for design 6 through 9 were confounded by d_1/X_2 and taper angle as defined in Table 1. The taper angle differences were a result of the experimental DRIE etching process used. Alam et al. suggest that reducing the taper angle on an orifice should increase the discharge coefficient for thick walled orifices (Alam et al., 2016). A limitation of the study by Alam et al. as it applies to this work is that angles of 30 through 75 degrees were studied, whereas angles from 0.4 to 5.4 degrees were observed in designs 6 through 9. Given the confounded nature of results from designs 6 through 9, the only conclusion drawn from these studies was indifference of C_D with relation to number of orifices used.

Fluid system related impacts aside, increasing the number of same sized micro-orifices in a system similar to the scale of the micro-orifices tested in this work should give a linear increase in flow capacity. The close fitting percent differences between the numerical and experimental C_D data for the micro-orifice arrays showed that for micro-orifice arrays with micro-orifices separated by $2d_1$ or greater, the flow rate of each individual micro-orifice can be treated as discrete and used to sum to the expected flow capacity. It should be noted that this inter-orifice spacing was chosen to maintain mechanical integrity of the orifice plates. As stress concentrations in thin plates with orifices extend radially from an orifice edge by $1.5d_1$, reducing inter-orifice spacing to less than $2d_1$ makes orifice plates using materials such as silicon likely to fail at pressure differences studied within this work. For completeness, it is noted that the inter-orifice spacing was not an explicitly varied parameter studied.

It is also of note that discharge coefficient values for the tested micro-orifice arrays trended towards $C_D = 1$ when thin orifice plates, $X_1 = 525 \, \mu \text{m}$, were used. Similar results were observed by Mishra and Peles (2005b) and Kayser and Shambaugh (1991) for micro-orifices. In comparison, relatively thicker orifice plates seemed to lead to lower C_D . This is evident when comparing orifice plate design 1 as shown in Fig. 8 to orifice plate design 6 as shown in Fig. 9.

In addition to flow rate testing, the shock structures observed through schlieren imaging matched the shock structures found in numerical results closely. Observed shock structures suggested that the micro-orifices acted like under expanded micronozzles at most pressure ratios as shown in Fig. 22 for the 350 μm micro-orifices. Equivalence between the numerical models and schlieren imaging support that the numerical domain used was equivalent to the experimental domain. This being known, combined with supporting data from flow rate testing suggests that with the spacing between micro-orifices used, $>2d_1$, it is accurate to model an array of micro-orifices as a series of discrete micro-orifices, each modeled using a two dimensional axisymmetric domain.

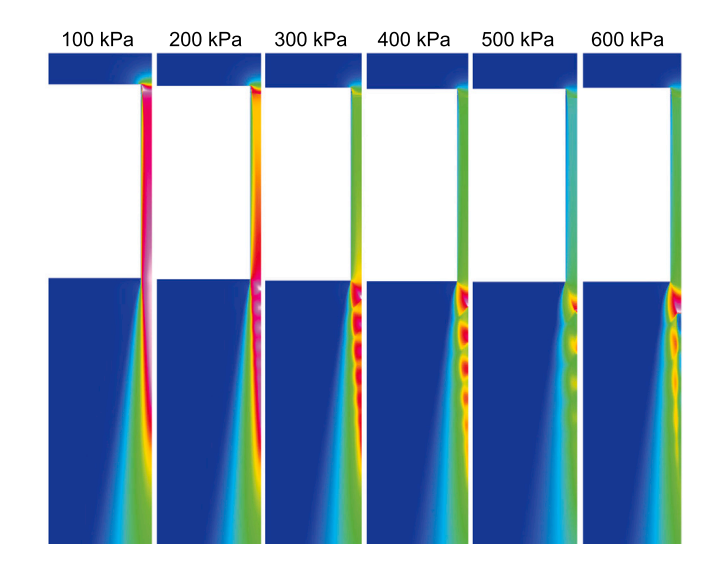


Fig. 22. $350 \mu m$ orifice velocity contours at gauge inlet pressures ranging from 100 kPa to 600 kPa. (For interpretation of the references to color in this figure legend, the reader is referred to the web version of this article.)

6. Conclusion

The studies conducted within the scope of this work provide a method for understanding micro-orifice array flow rate behavior. To do this, an experimental study was planned in coordination with numerical modeling to analyze the flow rates and shock structures present in jet flow of various micro-orifice array designs. The experimental work consisted of flow rate testing using a test bench for flow rate characterization of pneumatic components as well as a schlieren imaging system developed for small scale flow fields. Numerical work consisted of developing a set of two dimensional axisymmetric models to mirror experimental conditions. The numerical models were cross-validated with both the flow rate data and with the schlieren data.

The studies concluded with three key findings. First, given sufficient spacing between micro-orifices in a micro-orifice array, it is accurate to numerically model a three dimensional array of micro-orifices as a series of two dimensional axisymmetrically modeled micro-orifices. Second, micro-orifice aspect ratio plays a minor but significant role in determining C_D for a given micro-orifice or micro-orifice array. Finally, design of micro-orifices with C_D as high as 0.997 is possible through use of a photochemical etching process. In combination, these conclusions provide sufficient information to design highly efficient micro-orifice arrays for use in microscale and macroscale transport systems.

CRediT authorship contribution statement

Nathan P. Hagstrom: Conceptualization, Data curation, Formal analysis, Investigation, Methodology, Resources, Software, Validation, Visualization, Writing – original draft, Writing – review & editing. Matthew L. Gallagher: Formal analysis, Resources, Writing – review & editing. Thomas R. Chase: Supervision, Formal analysis, Resources, Writing – review & editing.

Declaration of competing interest

The authors declare the following financial interests/personal relationships which may be considered as potential competing interests: Thomas Chase reports financial support was provided by National Fluid Power Association. Nathan Hagstrom has patent #US11067187B2 issued to University of Minnesota. Thomas Chase has patent #US10330212B2 issued to University of Minnesota.

Data availability

Data will be made available on request.

Acknowledgments

This material is based on work supported by the National Science Foundation, United States under Grant PFI-2016330 and Grant I-CORPS-1940068, and by the National Fluid Power Association Education and Technology Foundation, United States. Portions of this work were conducted in the Minnesota Nano Center, which is supported by the National Science Foundation, United States through the National Nano Coordinated Infrastructure Network (NNCI) under Award Number ECCS-1542202. Mr. John Xiong is acknowledged for his assistance in manufacturing the silicon orifice plate samples.

References

- Alam, M., Setoguchi, T., Matsuo, S., Kim, H., 2016. Nozzle geometry variations on the discharge coefficient. Propuls. Power Res. 5 (1), 22–33.
- Aly, A.A.E.-A., Chong, A., Nicolleau, F., Beck, S., 2010. Experimental study of the pressure drop after fractal-shaped orifices in turbulent pipe flows. Exp. Therm Fluid Sci. 34 (1), 104–111.
- Aniskin, V., Mironov, S., Maslov, A., 2013. Investigation of the structure of supersonic nitrogen microjets. Microfluid. Nanofluid. 14 (3-4), 605-614.
- Anon, 1989. ISO 6358:1989(E) Pneumatic Fluid Power Components Using Compressible Fluids Determination of Flow-Rate Characteristics. Standard, International Organization for Standardization, Geneva, CH.
- Asako, Y., Pi, T., Turner, S.E., Faghri, M., 2003. Effect of compressibility on gaseous flows in micro-channels. Int. J. Heat Mass Transfer 46 (16), 3041–3050.
- Au, A.K., Lai, H., Utela, B.R., Folch, A., 2011. Microvalves and micropumps for BioMEMS. Micromachines 2 (2), 179–220.
- Bharadwaja, R., Murugan, A., Chen, Y., Liou, F.W., 2019. Application of schlieren technique in additive manufacturing: A review. In: 2019 International Solid Freeform Fabrication Symposium. University of Texas at Austin.
- Chang, B., Leussink, P., Jensen, F., Hübner, J., Jansen, H., 2018. DREM: Infinite etch selectivity and optimized scallop size distribution with conventional photoresists in an adapted multiplexed bosch DRIE process. Microelectron. Eng. 191, 77–83.
- Cioncolini, A., Cassineri, S., Duff, J., Curioni, M., Scenini, F., 2018. Micro-orifice single-phase flow at very high Reynolds number. Exp. Therm Fluid Sci. 91, 35–40.
- Cioncolini, A., Scenini, F., Duff, J., 2015. Micro-orifice single-phase liquid flow: pressure drop measurements and prediction. Experimental Thermal and Fluid Science 65, 33–40.
- Cioncolini, A., Scenini, F., Duff, J., Szolcek, M., Curioni, M., 2016. Choked cavitation in micro-orifices: An experimental study. Exp. Therm Fluid Sci. 74, 49–57.
- Evgenevna, I.E., Evgenevna, I.T., Viktorovich, B.P., 2014. Analysis of the application of turbulence models in the calculation of supersonic gas jet. Am. J. Appl. Sci. 11 (11), 1914–1920.
- Galambos, P., Lantz, J., Baker, M.S., McClain, J., Bogart, G.R., Simonson, R.J., 2011.
 Active MEMS valves for flow control in a high-pressure micro-gas analyzer. J.
 Microelectromech. Syst. 20 (5), 1150–1162.
- Hagstrom, N.P., Fikru, N., Hargus, A.M., Chase, T.R., 2019. A novel piezoelectrically driven miniature proportional pneumatic control valve utilizing a microfabricated orifice array. IEEE/ASME Trans. Mechatronics 24 (5), 1931–1941.
- Hasegawa, T., Suganuma, M., Watanabe, H., 1997. Anomaly of excess pressure drops of the flow through very small orifices. Phys. Fluids 9 (1), 1–3.
- Ho, C.-M., Tai, Y.-C., 1998. Micro-electro-mechanical-systems (MEMS) and fluid flows. Annu. Rev. Fluid Mech. 30 (1), 579–612.
- Huang, C., Gregory, J.W., Sullivan, J.P., 2007a. Flow visualization and pressure measurement in micronozzles. J. Vis. 10 (3), 281–288.
- Huang, C., Gregory, J.W., Sullivan, J.P., 2007b. A modified schlieren technique for micro flow visualization. Meas. Sci. Technol. 18 (5), N32.
- Huang, S., Ma, T., Wang, D., Lin, Z., 2013. Study on discharge coefficient of perforated orifices as a new kind of flowmeter. Exp. Therm Fluid Sci. 46, 74–83.
- Jankowski, T., Schmierer, E., Prenger, F., Ashworth, S., 2008. A series pressure drop representation for flow through orifice tubes. J. Fluids Eng. 130 (5).

- Jin, Z.-j., Gao, Z.-x., Li, X.-j., Qian, J.-y., 2019. Cavitating flow through a micro-orifice. Micromachines 10 (3), 191.
- Kayser, J.C., Shambaugh, R.L., 1991. Discharge coefficients for compressible flow through small-diameter orifices and convergent nozzles. Chem. Eng. Sci. 46 (7), 1697–1711.
- Kleine, H., 2001. Measurement techniques and diagnostics. In: Ben-Dor, G., Igra, O., Elperin, T. (Eds.), Handbook of Shockwaves Volume 1: Theoretical, Experimental, and Numerical Techniques. Academic Press, pp. 683–785.
- Lekholm, V., Palmer, K., Thornell, G., 2012. Schlieren imaging of microthruster exhausts for qualitative and quantitative analysis. Meas. Sci. Technol. 23 (8), 085403.
- Lekholm, V., Rämme, G., Thornell, G., 2011. Seeing the invisible with schlieren imaging. Phys. Educ. 46 (3), 294.
- Menter, F.R., Langtry, R.B., Likki, S., Suzen, Y., Huang, P., Völker, S., 2006. A correlation-based transition model using local variables—part I: model formulation. J. Turbomach. 128 (3), 413–422.
- Mishra, C., Peles, Y., 2005a. Cavitation in flow through a micro-orifice inside a silicon microchannel. Phys. Fluids 17 (1), 013601.
- Mishra, C., Peles, Y., 2005b. Incompressible and compressible flows through rectangular microorifices entrenched in silicon microchannels. J. Microelectromech. Syst. 14 (5), 1000–1012.
- Mueller, J., Chakraborty, I., Vargo, S., Marrese, C., White, V., Bame, D., Reinicke, R., Holzinger, J., 2000. Towards micropropulsion systems on-a-chip: initial results of component feasibility studies. In: Aerospace Conference Proceedings, Vol. 4. IEEE, pp. 149–168.
- Nazari, A.Z., Ishino, Y., Ishiko, Y., Ito, F., Kondo, H., Yamada, R., Motohiro, T., Miyazato, Y., Nakao, S., et al., 2020. Multi-schlieren CT measurements of supersonic microjets from circular and square micro nozzles. J. Flow Control Meas. Vis. 8 (03), 77.
- Oh, K.W., Ahn, C.H., 2006. A review of microvalves. J. Micromech. Microeng. 16 (5), R13-R39
- Park, J.M., Evans, A.T., Rasmussen, K., Brosten, T.R., Nellis, G.F., Klein, S.A., Gianchandani, Y.B., 2009. A microvalve with integrated sensors and customizable normal state for low-temperature operation. J. Microelectromech. Syst. 18 (4), 868–877.
- Park, J.M., Taylor, R.P., Evans, A.T., Brosten, T.R., Nellis, G.F., Klein, S.A., Feller, J.R., Salerno, L., Gianchandani, Y.B., 2008. A piezoelectric microvalve for cryogenic applications. J. Micromech. Microeng. 18 (1), 015023.
- Phalnikar, K., Kumar, R., Alvi, F., 2008. Experiments on free and impinging supersonic microiets. Exp. Fluids 44 (5), 819–830.
- Rienitz, J., 1975. Schlieren experiment 300 years ago. Nature 254 (5498), 293-295.
- Saad, M.A., 1985. Compressible Fluid Flow. Prentice-Hall, Inc., Englewood Cliffs, NJ, p. 570.
- Saha, S., Leung, K.-F., Nguyen, T.D., Stoddart, J.F., Zink, J.I., 2007. Nanovalves. Adv. Funct. Mater. 17 (5), 685–693.
- Scroggs, S., Settles, G., 1996. An experimental study of supersonic microjets. Exp. Fluids $21\ (6),\ 401-409.$
- Settles, G.S., 2001. Schlieren and Shadowgraph Techniques: Visualizing Phenomena in Transparent Media. Springer Science & Business Media.
- Settles, G.S., Hargather, M.J., 2017. A review of recent developments in schlieren and shadowgraph techniques. Meas. Sci. Technol. 28 (4), 042001.
- Shoji, S., Esashi, M., 1994. Microflow devices and systems. J. Micromech. Microeng. 4 (4), 157–171.
- Su, X., Wu, J., Hinds, B.J., 2015. Nanoscale bubble valves on MWCNT membranes for chemical energy storage. Adv. Mater. Interfaces 2 (16), 1500102.
- Tang, Y., Sandoughsaz, A., Najafi, K., 2017. Ultra high aspect-ratio and thick deep silicon etching (UDRIE). In: 2017 IEEE 30th International Conference on Micro Electro Mechanical Systems. MEMS, IEEE, pp. 700–703.
- Vandelli, N., Wroblewski, D., Velonis, M., Bifano, T., 1998. Development of a MEMS microvalve array for fluid flow control. J. Microelectromech. Syst. 7 (4), 395–403.
- Vogt, E.C., 1957. The Design and Testing of an All-Lens Schlieren System. Tech. Rep., Texas Univ at Austin Defense Research Lab.
- White, F.M., 2008. Fluid Mechanics, sixth ed. McGraw-Hill, Boston, MA, pp. 617–618.Wright, S., Syms, R., 2018. Supersonic jet interactions with a micro-engineered skimmer. J. Micromech. Microeng. 28 (8), 085017.
- Yang, E.-H., Lee, C., Mueller, J., George, T., 2004. Leak-tight piezoelectric microvalve for high-pressure gas micropropulsion. J. Microelectromech. Syst. 13 (5), 799–807.
- Zhang, C., Xing, D., Li, Y., 2007. Micropumps, microvalves, and micromixers within PCR microfluidic chips: advances and trends. Biotech. Adv. 25 (5), 483–514.

This article was published in the International Journal of Heat and Fluid Flow, Vol 103, Hagstrom, Nathan P., Gallagher, Matthew L. & Chase, Thomas R., "Characterization of compressible flow through microscale orifice arrays", Article No 109173, Copyright Elsevier (2023).